Journal of Alloys and Compounds 785 (2019) 156–162

Contents lists available at ScienceDirect

Journal of Alloys and Compounds

journal homepage: http://www.elsevier.com/locate/jalcom

Electronic bandgap manipulation of monolayer WS_2 by vertically coupled insulated $Mg(OH)_2$ layers

Fang Wang [a], Anyang Cui [a], Huimin Sun [a], Bin Zhou [a], Liping Xu [a], Kai Jiang [a], Liyan Shang [a, **], Zhigao Hu [a, b, *], Junhao Chu [a]

[a] Key Laboratory of Polar Materials and Devices (MOE) and Technical Center for Multifunctional Magneto-Optical Spectroscopy (Shanghai), Department of Electronic Engineering, East China Normal University, Shanghai, 200241, China
[b] Collaborative Innovation Center of Extreme Optics, Shanxi University, Taiyuan, Shanxi 030006, China

ARTICLE INFO

Article history:
Received 9 November 2018
Received in revised form
5 January 2019
Accepted 11 January 2019
Available online 16 January 2019

Keywords:
WS_2
$Mg(OH)_2$
Fermi level
Heterostructures

ABSTRACT

Searching for novel two-dimensional (2D) materials with tunable electrical and optical properties is significant to develop next-generation multifunctional nanoscale optoelectronic devices. The new insulated $Mg(OH)_2$ is a promising and stable 2D material to construct heterojunction with transition metal dichalcogenides (TMDs). Here, WS_2-$Mg(OH)_2$ is experimentally designed and investigated. The similarity of lattice constants for the two materials is confirmed with selected area electron diffraction for the first time. By stacking $Mg(OH)_2$ layers on WS_2 monolayer, the Fermi level of WS_2 is distinctly elevated, making the WS_2-$Mg(OH)_2$ a promising heterostructure for constructing and optimizing tunable electronic devices. We also showed the adjustable transition properties with enhanced coupling effect by thinning the $Mg(OH)_2$ layers in the heterostructure. This study not only demonstrates the tunable Fermi levels and optical characteristics of WS_2-$Mg(OH)_2$, but also could promote the broad investigations of novel 2D materials for various optoelectronic device applications in nanoscale.

1. Introduction

Synthesized $Mg(OH)_2$, a member of alkaline-earth hydroxides (AEH) with formula $X(OH)_2$, (X = Mg or Ca), was studied as a new member of two-dimensional (2D) materials [1]. Magnesium or calcium hydroxides is one of the multifunctional materials, which has many important applications in industry, technology, solid-state electronics, and photovoltaic devices [2]. With strongly bonded hydrogen and oxygen atoms in -OH groups creating chemically passivated surfaces, the 2D AEH is stable in ambient conditions. The prolonged environmental stability has been determined by various approaches such as the surface morphology and structured analysis, where no sign of surface degradation was illustrated by Raman spectra within a three-month timeframe [3]. It is superior to metastable or unstable 2D materials such as silicene, black phosphorus, $MoTe_2$, and GaTe. However, the 2D $Mg(OH)_2$ has a band gap of around 5 eV, which greatly limits its application in semiconductor device field [2]. As a consequence, beyond being novel atomic-thick materials, lateral and vertical heterostructures of these 2D crystals should also be taken into account.

As constituents of possible heterostructures, transition metal dichalcogenides (TMDs) are very promising and attracting wide attention and research. Those new members of 2D monolayer materials possess tunable electronic properties from metallic to wide-gap semiconducting and excellent mechanical properties [4–7]. Moreover, TMDs have been used in various fields, such as hydrogen storage, photonics, nanoelectronics, catalysis, and Li-ion battery applications [8–12]. Among TMDs, WS_2 was reported to possess the lightest charge carriers and similar lattice constant with $Mg(OH)_2$, which significantly improves the electrical properties and reduces lattice mismatch between the two materials [2]. Therefore, it is meaningful and practical for $Mg(OH)_2$ to constructing heterostructures with WS_2 for enhanced functionalities.

Here, we experimentally and theoretically reported the formation, tuning, and characterization of WS_2-$Mg(OH)_2$ heterostructure. By stacking $Mg(OH)_2$ layers on WS_2 monolayer, the Fermi levels are

* Corresponding author. Key Laboratory of Polar Materials and Devices (MOE) and Technical Center for Multifunctional Magneto-Optical Spectroscopy (Shanghai), Department of Electronic Engineering, East China Normal University, Shanghai, 200241, China.
** Corresponding author.
E-mail addresses: lyshang@ee.ecnu.edu.cn (L. Shang), zghu@ee.ecnu.edu.cn (Z. Hu).

https://doi.org/10.1016/j.jallcom.2019.01.129
0925-8388/

distinctly elevated, making the WS_2-$Mg(OH)_2$ a promising heterostructure for constructing p-n junctions with WS_2 monolayer. The built-in potential of the p-n junctions is tunable as the Fermi levels of WS_2-$Mg(OH)_2$ increase with the thickness of $Mg(OH)_2$ layers. As a result, it is appropriate for WS_2-$Mg(OH)_2$ heterostructure to optimize tunable electronic devices with short depletion region. Furthermore, adjustable transition properties of WS_2 monolayer by stacking with $Mg(OH)_2$ layers of different thickness are revealed. Our results reveal that 2D material of $Mg(OH)_2$ combined with TMDs is an effective structure, and could lead to the emergence of novel multifunctional nanoscale optoelectronic devices.

2. Experimental section

2.1. Synthesis of WS_2-$Mg(OH)_2$ heterostructure

The WS_2 monolayers were grown by low-pressure chemical vapor deposition (CVD) technique for 15 min. The 285 nm SiO_2/Si substrates were cleaned using piranha solution (a volumetric mixture of 3:1 of 98% H_2SO_4 to 35% H_2O_2), then placed face down on the alumina boat which contains WO_3 powder. The alumina boat was placed inside the quartz tube in the second zone. The temperature of the second zone was raised up to 800 °C with a heating ramp of 10 °C min^{-1} and the deposition took place at 800 °C for 10 min. At the same time, the temperature of the first zone was also reached 200 °C so as to evaporate the sulfur powder. After the deposition, the furnace was allowed to cool naturally to room temperature. During the entire growth process, the argon flow rate was maintained at 80 SCCM. The good crystallinity and thickness for the monolayers are confirmed by the Raman mapping and atomic force microscope (AFM) topographies. The detailed growth process can be found in Ref. [6].

Analogues to graphene, few-layer $Mg(OH)_2$ flakes are obtained by overcoming the weak van der Waals interaction between layers in the bulk crystals. They are peeled by micromechanical cleavage using adhesive tape and applied to the substrates with large-area continuous WS_2 monolayers to prepare heterostructures. The synthetic WS_2-$Mg(OH)_2$ are optically identified by optical microscope. This method decreases the chance of redundant impurity being introduced into the heterostructure by transfer.

2.2. Optical and electronic characterizations

Temperature dependent Raman/PL experiments were carried out by a Jobin-Yvon LabRAM HR Evolution spectrometer and a THMSE 600 heating/cooling stage (Linkam Scientific Instruments) in the temperature range from liquid nitrogen temperature −196 °C to 77 °C with a resolution of 0.1 °C. The WS_2 monolayers was excited by the 532 nm line of a solid-state laser and recorded in back-scattering geometry with a resolution of better than 1 cm^{-1}. The laser beam was focused through a 50 × microscope with a working distance of 18 mm. The output power of the 532 laser was controlled to be 13.9 μW, which remains unchanged during the whole experimental process. An air-cooled CCD (−70 °C) with a 1024 × 256 pixels front illuminated chip was used to collect the scattered signal dispersed on 1800 grooves/mm grating for Raman and 300 grooves/mm grating for PL, respectively.

The topographies and surface potential distributions were investigated via an AFM (Dimension Icon, Bruker) with Pt/Ir-coated cantilevers in noncontact mode. An ac tip bias (2 kHz, 2000 mV) was applied here. The Kelvin probe force microscopy (KPFM) was used to quantitatively characterize the discrepant contact potential difference (CPD) distribution. We used Pt/Ir-coated with the cantilevers in the noncontact mode so that the topography and surface potential signal can be measured simultaneously with a mechanical drive frequency of 68.3 kHz and an AC modulation of 2 V at 2 kHz. Tip bias was adjusted to cancel out the capacitive force generated by the work function disparity of $\phi_{tip} - \phi_{sample}$ using the equation as $CPD \times e = \phi_{tip} - \phi_{sample}$. The ϕ_{tip} can be easily obtained if ϕ_{sample} for the gold film is assumed to be 5.4 eV. The work function of the probe is always calibrated in advance by scanning a gold plate, and the corresponding CPD resolution is −0.6 mV. Accordingly, the work function for the probe ϕ_{tip} is calibrated to be 4.8 eV. With the foregone ϕ_{tip}, the information of work function for samples can be derived by estimating the CPD distribution.

2.3. Computational details

The density functional theory (DFT) calculations were performed with plane-wave pseudopotentials from the calculate method of quantum mechanics [13,14]. The generalized gradient approximation (GGA) for exchange-correlation term was employed, and the functional was adopted for structure optimization and band gaps calculation [15]. The selected pseudopotential is Ultrasoft Pseudopotentials. To acquire accurate results for bilayer structures, DFT-D approach was included with the Ortmann-Bechstedt-Schmidt (OBS) vdW correction [16], which gives the structural parameters in good agreement with experimental values. Geometry optimization was determined using the Broyden-Fletcher-Goldfarb-Shenno (BFGS) minimization technique, with thresholds of converged structure of energy change per atom smaller than 10^{-5} eV/atom, and displacement of atoms during geometry optimization no more than 0.001 A. All calculations were carried out using a 1 × 1 supercell with vacuum thickness not smaller than 17 Å and spin-orbit coupling was not included.

3. Results and discussion

3.1. Surface morphologies for $Mg(OH)_2$ and WS_2

For the 2D $Mg(OH)_2$, it was fabricated successfully from its layered bulk crystals and has a wide direct-gap of about 5 eV [17]. Fig. 1 (a) shows the optical image of mechanically exfoliated $Mg(OH)_2$ flakes. When the material is thinned to mono- and few-layers (<10 layers), the shearing mode of the -OH group E_g^{OH} and the traditional breathing/shearing modes (A_{1g}/E_g) located at low frequency cannot be observed in Raman spectra. It is on account of low optical absorption coefficient of wide band gap $Mg(OH)_2$. However, the A_{1g}^{OH} mode at high frequency is experimental measurable. It is a breathing mode of the -OH group, which involves O and H atom motion along the out of plane direction when the alkaline atom is stationary [3]. Since both H and O atoms are relatively light, its peak position appears at very high frequencies (ω~3675 cm^{-1}). The presence of A_{1g}^{OH} peak for 2D $Mg(OH)_2$ can be clearly seen at 3675 cm^{-1} from Raman mapping with 532 nm laser in Fig. 1(c). The Raman intensity gradually decreases from thick to 2D regions due to weak scattering from the lessened amount of materials. The normalized temperature-dependent Raman spectra in Fig. 1(d) reveal almost no shift with temperature, which demonstrates the stability of the 2D $Mg(OH)_2$ flakes with chemically passivated surfaces. It makes $Mg(OH)_2$ flakes be considered as a promising fresh and stable materials for constituting vertical heterostructures. Transmission electron microscopy (TEM) image and selected area electron diffraction (SAED) pattern also confirm high crystallinity of the synthesized materials as shown in Fig. 1(e). The SAED pattern displays a hexagonal pattern and reveals the interplanar crystal spacing $d = 0.271$ and 0.471 nm, corresponding to the (100) and (001) facets of $Mg(OH)_2$. The corresponding energy

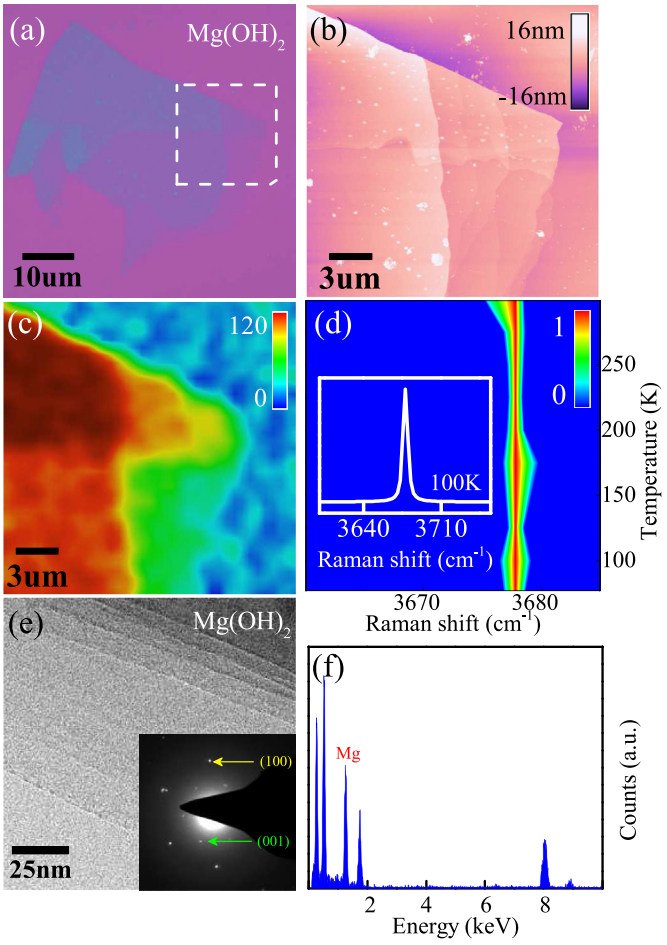

Fig. 1. (a) Optical microscope image of the mechanically exfoliated $Mg(OH)_2$ flakes; (b) The AFM topographies in the dashed frame region of panel (a); (c) Raman mapping under the confocal measurements in the dashed frame region of panels (a); (d) Temperature dependent Raman spectra of $Mg(OH)_2$ flakes. The insert shows the Raman spectrum at 100 K; (e) TEM image and SAED pattern taken from synthesized crystals; (f) EDX spectrum of $Mg(OH)_2$.

dispersive X-ray (EDX) further verifies the Mg element in $Mg(OH)_2$.

It was reported that the calculated lattice constants of the $Mg(OH)_2$ and WS_2 are very close, indicating that there is a slight lattice mismatch between the two materials [2]. As a result, WS_2 is outstanding in the TMDs for constructing heterostructures with $Mg(OH)_2$. Here, we synthesize the WS_2 monolayer, whose monolayer nature is confirmed with the hight map in AFM topography [Fig. 2(a)]. It's corresponding optical image is in the upper left corner. The Raman mapping of the A_{1g} mode for WS_2 [Fig. 2(b)] indicates the high quality of the sample. Fig. 2(c) shows high resolution TEM images of WS_2 exhibiting the hexagonal lattice. The monocrystalline nature of the sample is confirmed by the SAED pattern in the corner. The interplanar crystal spacing $d = 0.273$ nm corresponds to the (100) facets of WS_2. The EDX of W element is listed in Fig. 2(d), which confirms the sample is W based. It is noteworthy that the interplanar crystal spacings for (100) facets of WS_2 (0.273 nm) and $Mg(OH)_2$ (0.271 nm) are quite close. This finding confirms the similarity of lattice constants for $Mg(OH)_2$ and WS_2 experimentally for the first time.

3.2. Manipulation of surface potential for monolayer WS_2 with vertically stacked $Mg(OH)_2$

Here, we exfoliated the $Mg(OH)_2$ flakes on the large-area

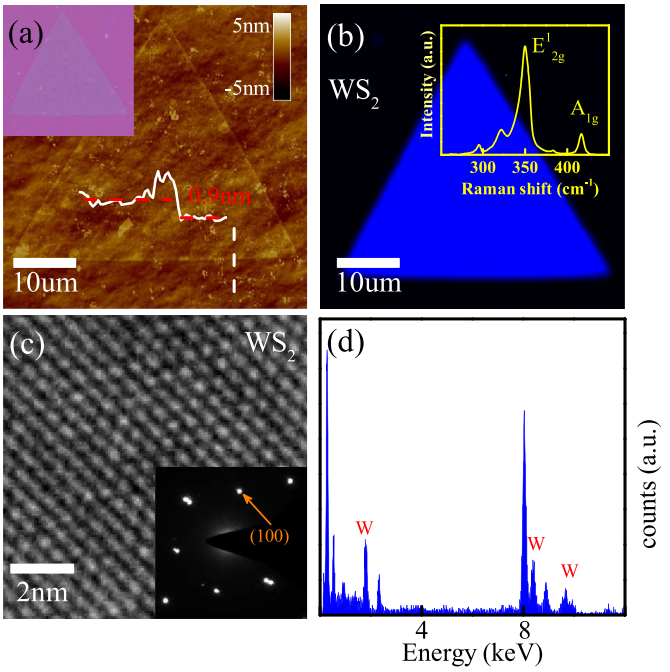

Fig. 2. (a) The AFM topography of WS_2, confirming the monolayer nature of the samples. The inset shows the optical image of WS_2 monolayer; (b) Raman mapping at 417 cm^{-1} (A_{1g} mode in WS_2) of the WS_2 monolayer; The inset illustrates the Raman spectrum of WS_2 excited by the 532 nm laser; (c) High-resolution TEM image and SAED pattern for WS_2; (d) EDX spectrum of WS_2.

continuous WS_2 monolayers to prepare the WS_2-$Mg(OH)_2$ heterostructure, which is attributed to the mature synthetic conditions and excellent method of mechanical exfoliation. This method decreases the chance of redundant impurity being introduced into the heterostructure by transfer. The optical microscope image of the vertical WS_2-$Mg(OH)_2$ heterostructure is revealed in Fig. 3(a). The whole background is the monolayer of large area WS_2 by CVD. The pattern on the background displays WS_2 stacked with $Mg(OH)_2$ of 3 layers, 9 layers, and 15 layers, which has been confirmed by the AFM topographies and hight map in Fig. 3(c) and (e). When the WS_2 monolayer is overlapped with the stacking flakes, the Raman intensity is reduced [18]. However, the thickness of the $Mg(OH)_2$ layers has no significant influence on the intensity of WS_2-$Mg(OH)_2$ heterostructures. It can be extracted distinctly from the intensity-dependent Raman mapping at 416.7 cm^{-1} (A_{1g} mode in WS_2)of the heterostructure in Fig. 3(b). The corresponding Raman spectra of the points from WS_2 monolayer, WS_2-3L $Mg(OH)_2$, WS_2-9L $Mg(OH)_2$, and WS_2-15 L $Mg(OH)_2$ (WS_2 monolayer stacked with $Mg(OH)_2$ of three layers, nine layers, and 15 layers) are displayed in Fig. S1. This phenomenon may due to the involved intervalley scattering of electron or hole by phonons with large momenta in $Mg(OH)_2$ [19].

In order to illustrate the internal electrical structure of WS_2-$Mg(OH)_2$ heterostructure, the discrepant contact potential difference (CPD) distribution for the heterostructure is further recorded with Kelvin probe force microscopy (KPFM)(Dimension Icon, Bruker), which is widely employed to probe the local variations in the work functions of various surfaces [20]. From Fig. 3(c) and (d), the sample topographies and surface potential images match perfectly, which is rarely seen for the in-plane heterostructure [20]. Due to the long depletion region for the in-plane heterostructure, the contrast feature of KPFM image is generally different from the topographic image. The sharp boundary in Fig. 3(d) reveals the short depletion region between WS_2 and the vertically stacked

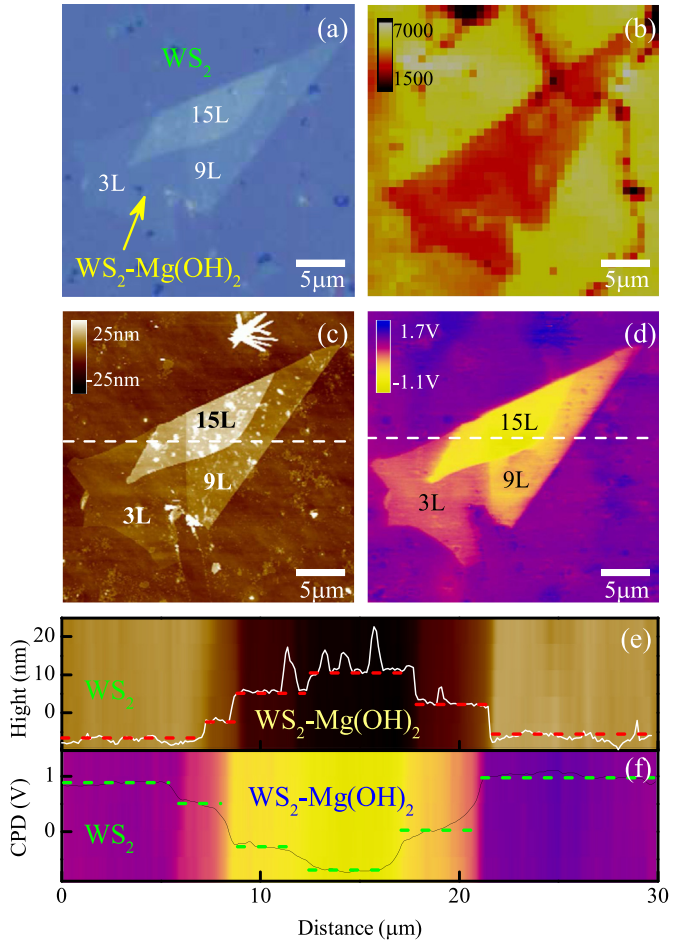

Fig. 3. (a) Optical microscope image of the vertical WS_2-$Mg(OH)_2$ heterostructure; (b) Raman mapping at 416.7 cm^{-1} (A_{1g} mode in WS_2) in the confocal measurements of heterostructure corresponding to panel (a); (c) The AFM topographies of the heterostructure; (d) The surface potential images of WS_2-$Mg(OH)_2$; (e) Cross-sectional height profiles of the $Mg(OH)_2$ on WS_2 corresponding to the region in the dashed line of panel (c); (f) The built-in potential distributions across the heterostructure corresponding to the dashed line in panel (d).

heterostructure, which is a promising characteristic for constructing efficient p-n junctions. The mapping of the work function also provides information about the composition and electronic states of the local structures from the WS_2 monolayer and WS_2-$Mg(OH)_2$ vertical heterostructure. The Fermi levels of WS_2 and the heterostructure can be estimated from the surface potential map, in order to obtain the scale of the space charge region, the value of built-in potential and so on. The CPD between the KPFM tip and the local area of WS_2 or heterostructure can be written as $CPD_{WS_2} \times e = \phi_{tip} - \phi_{WS_2}$ and $CPD_{hetero} \times e = \phi_{tip} - \phi_{hetero}$. Here, ϕ_{tip}, ϕ_{WS_2} and ϕ_{hetero} are the work functions of the tip, WS_2, and heterostructure, respectively. The ϕ_{tip} is calibrated to be 4.8 eV, which is acquired by scanning the standard sample of gold film. The difference between the Fermi levels of WS_2 and the heterostructure is obtained by measuring the $\Delta CPD_{WS_2-hetero}$ on average, which is defined as $\Delta E_F = \phi_{hetero} - \phi_{WS_2} = (CPD_{WS_2} - CPD_{hetero}) \times e = \Delta CPD_{WS_2-hetero} \times e$. As shown in Fig. 3(f), we found that the value of CPD_{hetero} is less than CPD_{WS2}. Thus, Fermi levels of the heterostructure region are higher than those of the monolayer WS_2. Moreover, the increasing layers of the $Mg(OH)_2$ will elevate the Fermi levels of the heterostructure. Consequently, monolayer WS_2 and WS_2-$Mg(OH)_2$ heterostructure can serve as p-n junctions, where WS_2 is on duty for p-side and WS_2-$Mg(OH)_2$ is on duty for n-side. Furthermore, the built-in potential of the p-n junctions is tunable as the Fermi levels of WS_2-$Mg(OH)_2$ increases with the thickness of $Mg(OH)_2$ layers. The built-in potential will lead to effective charge transfer, with the separated electrons and holes residing in two regions that can have a dominating effect on both photovoltaic responses and light emission. As a result, WS_2-$Mg(OH)_2$ is a promising heterostructure for constructing and optimizing photovoltaic devices.

For the purpose of looking further into the internal excitonic light emission, the luminescence characteristics for monolayer WS_2 and WS_2-$Mg(OH)_2$ heterostructure are revealed in Fig. 4. The WS_2-$Mg(OH)_2$ heterostructure forms a type II band alignment of ~1 eV, where the valence band maximum (VBM) and conduction band minimum (CBM) of $Mg(OH)_2$ are higher than that of WS_2 (Fig. 4 (a)) [2]. In type II heterojunctions, the CBM and VBM reside in two materials and spatially separated charge carriers can be formed. As a result, the type II band alignment and built-in potential in the heterojunctions can facilitate the photoexcited electron-hole separation and lead to an enhanced photoswitching performance [21]. Fig. 4 (b) shows that the WS_2 monolayer has a direct bandgap about 1.9 eV at the K-point. The calculated band structure and density of states for WS_2-$Mg(OH)_2$ in Fig. 4 (c) shows that the VBM of the heterojunction lying at the Γ point originates from $Mg(OH)_2$. It exclusively consists of p_x and p_y orbitals of the O atoms. While the CBM of the structure at the K point arises from the WS_2 layer, which is characterized by the orbitals of W and S atoms. Furthermore, the band structure of the WS_2 in the heterostructure is disturbed by the coupling effect of $Mg(OH)_2$. It results in the narrowing of band gap in WS_2. From the PL mapping (Fig. 4 (e)) corresponding to the optical microscope image in Fig. 4 (d), it can be obtained that the transition for the WS_2-$Mg(OH)_2$ experiences a red shift from WS_2 monolayer. The shift is more obvious from the PL spectra in Fig. 4 (d), which is extracted from the WS_2 parts and heterostructure area. Here, the PL peak for WS_2 has to be fitted with three peaks. Because the fitting results with two peaks can not match the original spectra, which is shown in Fig. S2. As displayed in Fig. 4 (f), the intrinsic transition for WS_2 monolayer is split into the neutral exciton (higher energy A^0) and charged exciton or trion (lower energy A^-), which originate from the transition of WS_2 in Fig. 4 (b) and (c) [22–25]. By comparing the PL spectra for WS_2 and WS_2-$Mg(OH)_2$ in Fig. 4 (f), it is obvious that both the neutral exciton A^0 and charged exciton A^- in WS_2 shift to the lower energy after stacking the $Mg(OH)_2$ layers. The transition offsets indicate the disturbance of band structure for WS_2 in the heterojunction. In addition to this conventional phenomenon, an extra peak at lower energy (labelled as L) is observed. It is most possible to be attributed to the defect sites in consideration of the large linewidth of peak L, which is almost over 150 meV.

3.3. Coupling behavior for WS_2 and $Mg(OH)_2$ with different thickness

To provide an insight on the coupling effect of WS_2 and $Mg(OH)_2$ with different layers in Figs. 3 and 4, detailed variable temperature PL spectra are performed. The PL intensity reveals obvious quenching effect with increasing temperature for WS_2-3L $Mg(OH)_2$, WS_2-9L $Mg(OH)_2$, and WS_2-15 L $Mg(OH)_2$ in Fig. 5(a), (b), and (c). The obvious decreasing of intensity is on account of the exponential increasing of the nonradiative electron-hole recombination rate [26]. The nonradiative channels, such as trapping by surface/defect/ionized impurity states, become thermally activated with increasing the temperature. The nonradiative lifetime τ_{NR} is

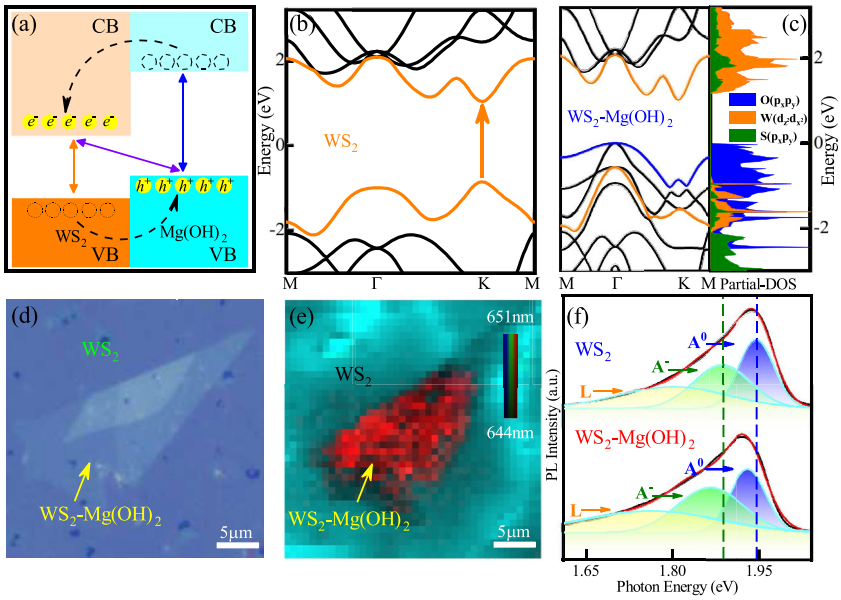

Fig. 4. (a) Schematic of the band alignment for type II heterostructure. (b) Theoretical electronic band structure of WS_2 monolayer. (c) The band structure (left) and corresponding partial density of states (right) of the vertical WS_2-$Mg(OH)_2$ heterostructure; (d) Optical microscope image of the vertical WS_2-$Mg(OH)_2$ heterostructure; (e) PL mapping in the confocal measurements of WS_2-$Mg(OH)_2$; (f) Multiple-peak fitting to experimental PL spectra of WS_2 and heterostructure.

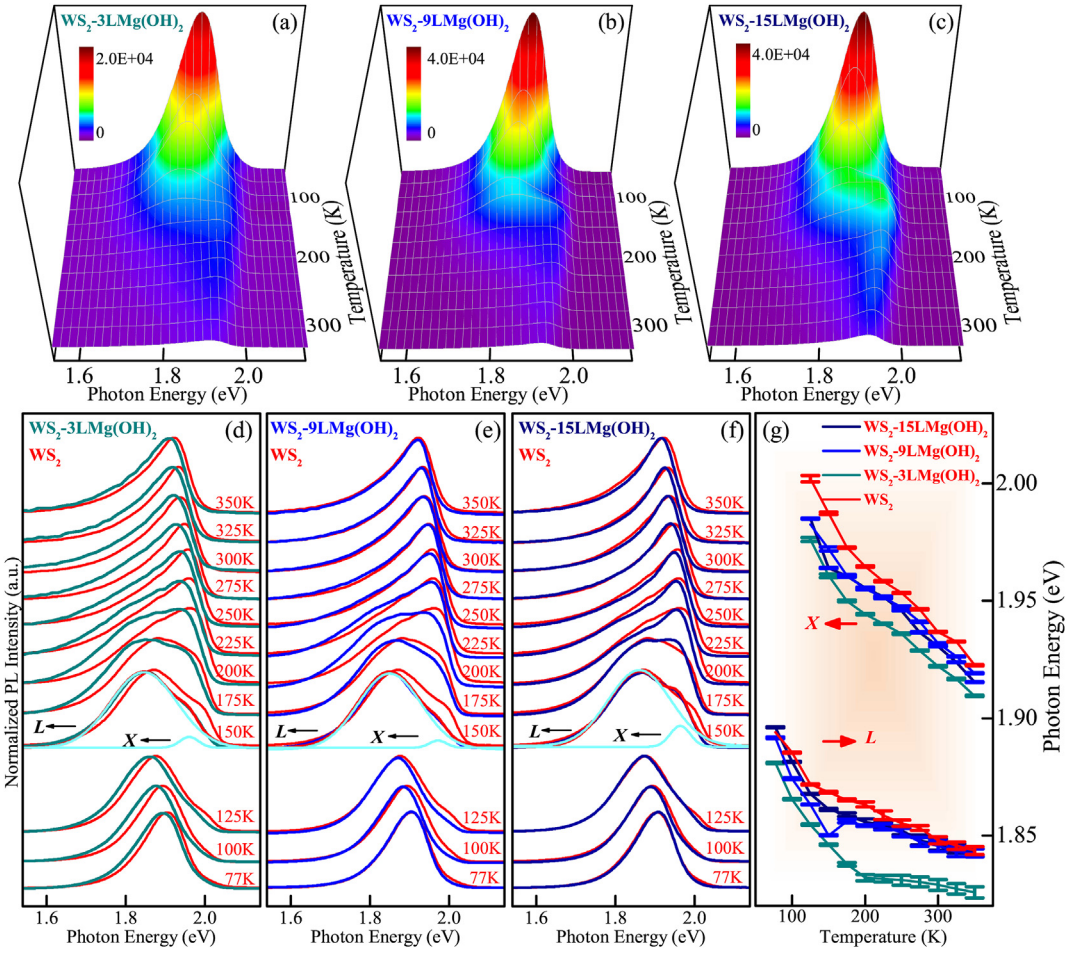

Fig. 5. (a) Graphic model of temperature dependent PL spectra for WS_2-$3LMg(OH)_2$; (b) Graphic model of WS_2-$9LMg(OH)_2$; (c) Graphic model of WS_2-$15LMg(OH)_2$; (d), (e), and (f) Normalized PL spectra of WS_2-$3LMg(OH)_2$, WS_2-$9LMg(OH)_2$, and WS_2-$15LMg(OH)_2$, respectively. The red line is the normalized PL spectra of WS_2 monolayer; (g) The transition excitons of WS_2-$3LMg(OH)_2$ (green), WS_2-$9LMg(OH)_2$ (light blue), and WS_2-$15LMg(OH)_2$ WS_2 (dark blue). The spectra of heterostructures are fitted with intrinsic transition exciton (*X*) and defect related exciton (*L*). (For interpretation of the references to colour in this figure legend, the reader is referred to the Web version of this article.)

expressed as $\tau_{NR} = \tau_0 \exp\left(\frac{E_a}{k_B T}\right)$ [18], where τ_0 is the pre-exponential factor, E_a is the activation energy in the thermal quenching process and k_B is the Boltzmann constant. As a result, the decreasing τ_{NR} with increasing temperature leads to the luminescence quenching, which can be expressed as $I = I_0 / \left[1 + A \exp\left(-\frac{E_a}{k_B T}\right)\right]$ [27], where I_0 is the intensity at 0 K, A is a parameter related to radiative lifetime (τ_R) as $A = \tau_R / \tau_0$, and τ_R is the radiative lifetime.

With the exception of the quenching effect with increasing the temperature, the defect related exciton L for the large area WS_2 is especially evident at low temperature. It can be seen from the red lines in the normalized PL of Fig. 5(d), (e), and (f). That is because the thermal energy at low temperature is not enough to avoid the trapping of the free mobile excitons in defect sites, and hence they can be localized/trapped and recombine radiatively to emit photons.

Obviously, the transitions in WS_2-$Mg(OH)_2$ heterojunctions have a red shift from WS_2 monolayer during the whole temperature changing process. It is attributed to the easily disturbed electronic band structure in TMDs [28,29]. As a result, the stacked coupling medium for WS_2 monolayer is an important factor to manipulate the electronic bandgap, no matter the coupling medium is homogeneous or heterogeneous [30,31]. Furthermore, some differences emerge when the thickness of the $Mg(OH)_2$ changes. For the purpose of making comparison among WS_2 and heterojunctions with $Mg(OH)_2$ layers of different thickness, we fitted the transition exciton A^0 and trion A^- with one peak X. The fitting results are displayed in Fig. 5(g), which make it clear that the coupling effect is stronger for thinner $Mg(OH)_2$ with WS_2 monolayers. When WS_2 is stacked with $Mg(OH)_2$ of three layers, the intrinsic exciton X is far away from the original position (the red fitting curve for WS_2) under the coupling effect. With the increasing thickness of $Mg(OH)_2$, the redshift of the heterojunctions is weakened (the dark and light blue fitting curve for WS_2-9L $Mg(OH)_2$ and WS_2-15 L $Mg(OH)_2$). The difference of shift between WS_2-9L $Mg(OH)_2$ and WS_2-15 L $Mg(OH)_2$ is much less than that for WS_2-3L $Mg(OH)_2$. It indicates that the band transition of the WS_2 monolayer is easily disturbed by the stacking materials. However, the disturbance is reduced when the amount of molecule for the heterogeneous materials is increasing. Band offsets in the heterojunction are expected to efficiently separate charge carriers or rectify charge flow, offering a mechanism for designing atomically thin devices and probing exotic two-dimensional physics [31]. As a consequence, the larger transition offsets by more serious disturbance from thinner $Mg(OH)_2$ is more appropriate for constructing heterojunction with stronger coupling effect, which could advance the electronic devices.

4. Conclusion

In conclusion, the electronic and optical properties of the WS_2-$Mg(OH)_2$ heterostructure have been investigated. We found that the Fermi level of WS_2 monolayer is elevated with increasing layers of $Mg(OH)_2$ under the effect of dielectric impact. Furthermore, the depletion region between WS_2 and the vertically stacked heterostructure becomes short. It makes WS_2-$Mg(OH)_2$ a promising heterostructure for constructing and optimizing photovoltaic devices. In addition, we conclude that the coupling effect can be enhanced when the thickness of $Mg(OH)_2$ is sheared thinner in the heterostructure. The present results highlight the significance of heterogeneous coupling and charge transfer in tuning the light emission and absorption of TMDs.

Acknowledgments

This work was financially supported by the National Key R&D Program of China (Grant Nos. 2018YFB0406500 and 2017YFA0303403), the National Natural Science Foundation of China (Grant Nos. 61674057 and 61227902), the Projects of Science and Technology Commission of Shanghai Municipality (Grant Nos. 18JC1412400, 18YF1407200, and 18YF1407000), the Program for Professor of Special Appointment (Eastern Scholar) at Shanghai Institutions of Higher Learning, the Fundamental Research Funds for the Central Universities.

Appendix A. Supplementary data

Supplementary data to this article can be found online at https://doi.org/10.1016/j.jallcom.2019.01.129.

References

[1] W. Xiong, C. Xia, J. Du, T. Wang, X. Zhao, Y. Peng, Z. Wei, J. Li, Electrostatic gating dependent multiple-band alignments in a high-temperature ferromagnetic $Mg(OH)_2/VS_2$ heterobilayer, Phys. Rev. B 95 (2017), 245408.
[2] M. Yagmurcukardes, E. Torun, R.T. Senger, F.M. Peeters, H. Sahin, $Mg(OH)_2$-WS_2 van der Waals heterobilayer: electric field tunable band-gap crossover, Phys. Rev. B 94 (2016), 195403.
[3] A. Suslu, K. Wu, H. Sahin, B. Chen, S. Yang, H. Cai, T. Aoki, S. Horzum, J. Kang, F.M. Peeters, S. Tongay, Unusual dimensionality effects and surface charge density in 2D $Mg(OH)_2$, Sci. Rep. 6 (2016) 20525.
[4] A. Castellanos-Gomez, M. Poot, A. Steele Gary, S.J. van der Zant Herre, N. Agraït, G. Rubio-Bollinger, Elastic properties of freely suspended MoS_2 nanosheets, Adv. Mater. 24 (2012) 772–775.
[5] S. Wu, S. Buckley, J.R. Schaibley, L. Feng, J. Yan, D.G. Mandrus, F. Hatami, W. Yao, J. Vučković, A. Majumdar, X. Xu, Monolayer semiconductor nanocavity lasers with ultralow thresholds, Nature 520 (2015) 69–72.
[6] H.M. Sun, J.Y. Wang, F. Wang, L.P. Xu, K. Jiang, L.Y. Shang, Z.G. Hu, J.H. Chu, Enhanced exciton emission behavior and tunable band gap of ternary $W(S_xSe_{1-x})_2$ monolayer: temperature dependent optical evidence and first-principles calculations, Nanoscale 10 (2018) 11553–11563.
[7] D. Kozawa, R. Kumar, A. Carvalho, K. Kumar Amara, W. Zhao, S. Wang, M. Toh, R.M. Ribeiro, A.H. Castro Neto, K. Matsuda, G. Eda, Photocarrier relaxation pathway in two-dimensional semiconducting transition metal dichalcogenides, Nat. Commun. 5 (2014) 4543.
[8] W. Xu, T. Wang, S. Wu, S. Wang, N-doped carbon-coated MoS_2 nanosheets on hollow carbon microspheres for high-performance lithium-ion batteries, J. Alloys Compd. 698 (2017) 68–76.
[9] L. Yin, S. Chai, J. Ma, J. Huang, X. Kong, P. Bai, Y. Liu, Effects of binders on electrochemical properties of the SnS_2 nanostructured anode of the lithium-ion batteries, J. Alloys Compd. 698 (2017) 828–834.
[10] Z. Yin, H. Li, H. Li, L. Jiang, Y. Shi, Y. Sun, G. Lu, Q. Zhang, X. Chen, H. Zhang, Single-layer MoS_2 phototransistors, ACS Nano 6 (2012) 74–80.
[11] K. Chang, W. Chen, l-Cysteine-Assisted synthesis of layered MoS_2/graphene composites with excellent electrochemical performances for lithium ion batteries, ACS Nano 5 (2011) 4720–4728.
[12] T. Drescher, F. Niefind, W. Bensch, W. Grünert, Sulfide catalysis without coordinatively unsaturated sites: hydrogenation, cis-trans isomerization, and H_2/D_2 scrambling over MoS_2 and WS_2, J. Am. Ceram. Soc. 134 (2012) 18896–18899.
[13] P. Hohenberg, W. Kohn, Inhomogeneous electron gas, Phys. Rev. 136 (1964) B864–B871.
[14] W. Kohn, L.J. Sham, Quantum density oscillations in an inhomogeneous electron gas, Phys. Rev. 137 (1965) A1697–A1705.
[15] J.P. Perdew, Y. Wang, Accurate and simple analytic representation of the electron-gas correlation energy, Phys. Rev. B 45 (1992) 13244–13249.
[16] F. Ortmann, F. Bechstedt, W.G. Schmidt, Semiempirical van der Waals correction to the density functional description of solids and molecular structures, Phys. Rev. B 73 (2006), 205101.
[17] T. Murakami, T. Honjo, T. Kuji, DOS calculation analysis of new transparent conductor $Mg(OH)_2$-C, Mater. Trans. 52 (2011) 1689.
[18] F. Wang, J.Y. Wang, S. Guo, J.Z. Zhang, Z.G. Hu, J.H. Chu, Tuning coupling behavior of stacked heterostructures based on MoS_2, WS_2, and WSe_2, Sci. Rep. 7 (2017) 44712.
[19] Q. Qian, Z. Zhang, K.J. Chen, Layer-dependent second-order Raman intensity of MoS_2 and:WSe_2 influence of intervalley scattering, Phys. Rev. B 97 (2018) 165409.
[20] K. Chen, X. Wan, J. Wen, W. Xie, Z. Kang, X. Zeng, H. Chen, J.-B. Xu, Electronic properties of MoS_2-WS_2 heterostructures synthesized with two-step lateral epitaxial strategy, ACS Nano 9 (2015) 9868–9876.
[21] N. Huo, J. Yang, Le Huang, Z. Wei, S. Li, S. Wei, J. Li, Tunable polarity behavior and self-driven photoswitching in p-WSe_2/n-WS_2 heterojunctions, Small 11

(2015) 5430–5438.
[22] X. Wang, P. Wang, J. Wang, W. Hu, X. Zhou, N. Guo, H. Huang, S. Sun, H. Shen, T. Lin, M. Tang, L. Liao, A. Jiang, J. Sun, X. Meng, X. Chen, W. Lu, J.H. Chu, Ultrasensitive and broadband MoS_2 photodetector driven by ferroelectrics, Adv. Mater. 27 (2015) 6575–6581.
[23] Y. Wang, C. Cong, W. Yang, J. Shang, N. Peimyoo, Y. Chen, J. Kang, J. Wang, W. Huang, T. Yu, Strain-induced direct-indirect bandgap transition and phonon modulation in monolayer WS_2, Nano Res. 8 (2015) 2562–2572.
[24] Z. He, X. Wang, W. Xu, Y. Zhou, Y. Sheng, Y. Rong, J.M. Smith, J.H. Warner, Revealing defect-state photoluminescence in monolayer WS_2 by cryogenic laser processing, ACS Nano 10 (2016) 5847–5855.
[25] H.R. Gutierrez, N. Perea-Lopez, A.L. Elias, A. Berkdemir, B. Wang, R. Lv, F. Lopez-Urias, V.H. Crespi, H. Terrones, M. Terrones, Extraordinary room-temperature photoluminescence in triangular WS_2 monolayers, Nano Lett. 13 (2013) 3447–3454.
[26] E. Schubert, T. Gessmann, J. Kim, Light Emitting Diodes, Cambridge University Press, Cambridge, 2006. U.K.
[27] V.A. Fonoberov, K.A. Alim, A.A. Balandin, F. Xiu, J. Liu, Photoluminescence investigation of the carrier recombination processes in ZnO quantum dots and nanocrystals, Phys. Rev. B 73 (2006), 165317.
[28] S. Wang, S. Li, T. Chervy, A. Shalabney, S. Azzini, E. Orgiu, J.A. Hutchison, C. Genet, P. Samori, T.W. Ebbesen, Coherent coupling of WS_2 monolayers with metallic photonic nanostructures at room temperature, Nano Lett. 16 (2016) 4368–4374.
[29] A. Sikandar, M.F. Khan, M. Kyung-Ah, N. Ghazanfar, A. Amir Muhammad, D. Ghulam, A. Imtisal, S. Yongho, H. Suklyun, E. Jonghwa, Van der Waals heterojunction diode composed of WS_2 flake placed on p-type Si substrate, Nanotechnology 29 (2018), 045201.
[30] R. Schmidt, G. Berghauser, R. Schneider, M. Selig, P. Tonndorf, E. Malic, A. Knorr, S. Michaelis de Vasconcellos, R. Bratschitsch, Ultrafast coulomb-induced intervalley coupling in atomically thin WS_2, Nano Lett. 16 (2016) 2945–2950.
[31] S. Tongay, W. Fan, J. Kang, J. Park, U. Koldemir, J. Suh, D.S. Narang, K. Liu, J. Ji, J. Li, R. Sinclair, J. Wu, Tuning interlayer coupling in large-area heterostructures with CVD-grown MoS_2 and WS_2 monolayers, Nano Lett. 14 (2014) 3185–3190.